Continental Shelf Research 173 (2019) 56–72

Contents lists available at ScienceDirect

Continental Shelf Research

journal homepage: www.elsevier.com/locate/csr

Influences of sea level rise on tides and storm surges around the Taiwan coast

Wen-Cheng Liu[a,*], Wei-Che Huang[a,b]

[a] Department of Civil and Disaster Prevention Engineering, National United University, Miaoli 36063, Taiwan
[b] College of Engineering and Science, National United University, Miaoli 36063, Taiwan

ARTICLE INFO

Keywords:
Sea level rise (SLR)
Tide
Storm surge
Typhoon
Taiwan's coast
Advanced circulation model (ADCIRC)

ABSTRACT

Global sea level rise (SLR) rates are accelerating, and abnormal weather is occurring more frequently due to global warming and climate change. SLR could intensify coastal disasters and concerns of an increase in storminess. In this study, a two-dimensional advanced circulation model (ADCIRC) was used to simulate tides and storm surges around the Taiwan coast. The model was calibrated and verified using observed tides and storm surges at four tidal gauge stations, including Taipei Tamsui, Taichung Harbor, Kaohsiung Harbor, and Hualien Harbor, based on historical typhoon events. The root mean square error and skill value of the differences between the computed and observed water levels for model calibration and validation were in the range of 0.08–0.27 m and 0.92–0.99, respectively. The results showed a reasonable agreement between the simulated and observed tidal levels and surge heights. The validated model was then used to assess the impact of SLR on the tides and surge heights. Four typical typhoon events under present-day sea level conditions and under SLR conditions of 0.87 m and 1.9 m were used for the model simulations. The simulated results show that the largest differences in water levels and surge heights between present-day conditions and SLR of 0.87 m and 1.9 m are found at Taichung Harbor compared to other three-gauge stations. The changes in M_2 tidal amplitude are less than 1 cm due to sea level rise. Moreover, the timing of the M_2 tide was earlier by approximately 4.7 min and 9 min under SLR 0.87 m and 1.9 m, respectively, at Taichung Harbor. The maximum increases in water level ranged from 9.2 cm to 13.7 cm under SLR of 0.87 m and from 19.2 cm to 24.8 cm under SLR of 1.9 m at Taichung Harbor. The peak water level can significantly increase as a result of the SLR. All of these characteristics respond to an SLR with nonlinear and nonuniform behavior.

1. Introduction

Mean sea level rise (SLR) is one of the most discussed issues in climate change research. SLR can evidently affect coastal regions worldwide by posing such dangers as beach erosion, salt water intrusion into groundwater systems, coastal flooding, ecosystem imbalance, coastal habitat destruction, and infrastructure damage (Craft et al., 2009; Almas and Hygen, 2012; Mather and Stretch, 2012; Tang et al., 2013; Bilskie et al., 2014; Cheon and Suh, 2016; Sheng et al., 2016; Testut et al., 2016). SLR has been predicted by many scientists and researchers by means of hydrological, climatological, and/or dynamical models (e.g., Zuo and Oerlemans, 1997; Gregory and Oerlemans, 1998; Raper and Braithwaite, 2006). Recent projections of global SLR in the Intergovernmental Panel on Climate Change (IPCC) Fifth Assessment Report revealed that the possible SLR increase by 2100 would range from 0.26 to 0.98 m compared with the rise observed during 1986–2005 (Church et al., 2013; Bittermann et al., 2013). Church and White (2006, 2011) projected that the present rate of global SLR is approximately 1.9 mm/year and stated that this estimate could be expected to accelerate during the current century. Rahmstorf (2007) estimated that the rate of SLR would increase by 0.2–2 m in the year 2100. Scientists also suggested that a 1–5 m rise in sea level by 2100 is more realistic for several reasons, including the melting of ocean glaciers, disintegration of ice sheets, and thermal expansion of ocean water (Pfeffer et al., 2008; Bahar et al., 2009; Grinsted et al., 2010). Tseng et al. (2010) analyzed the patterns and trends of sea level rise in the regional seas around Taiwan using long-term tide gauges and satellite altimetry. The results showed that an average trend of 2.4 mm/year from 1961 to 2003 was larger than the reported global rate of 1.8 mm/year for the same period.

Global long-term tide-gauge data showed changes in the tides with the observed SLR (Ray, 2006, 2009; Jay, 2009; Woodworth, 2010), but

* Corresponding author.
E-mail address: wcliu@nuu.edu.tw (W.-C. Liu).

https://doi.org/10.1016/j.csr.2018.12.009
Received 30 September 2018; Received in revised form 16 December 2018; Accepted 21 December 2018
Available online 22 December 2018
0278-4343/

these changes were poorly captured by the global tidal models because of the coarse model resolution (Muller et al., 2011). A large impact of SLR on regional tides has been reported due to the high-resolution grids implemented compared to the results from coarse-resolution grids in the numerical models (Pickering et al., 2012; Hagen and Bacopoulos, 2012; Ward et al., 2012; Pelling et al., 2013; Atkinson et al., 2013). Recently, Lopes and Dias (2014) studied the influence of a local mean SLR on the tidal dynamics of a lagoon in Portugal and discovered that the tidal current magnitudes decreased toward the channel head for the present mean sea level and mean SLR, but the tidal current tended to increase with the mean SLR. Therefore, the tidal wave propagation would also significantly change with the mean rate of SLR. Zhao et al. (2014) investigated the influence of SLR on storm surges around the Changjiang Estuary. These researchers found that surges were not very sensitive to SLR, and the variations in water elevations could be attributed to changes in tides, with the extent of change ranging from several to a dozen centimeters. Luz Clara et al. (2015) applied the Model for Applications at Regional Scales (MARS) to probe the changes in tides atop the Patagonian continental shelf. The modeling results revealed that the tidal characteristics changed with the SLR as a result of the speed of tidal waves, the Rossby radius of deformation, dissipation of energy by bottom friction, and the resonant properties in the basin. Arns et al. (2015) used a Mike 21 model to investigate the impacts of the SLR on storm surge water levels in the northern part of the German Bight based on 65 extreme events that occurred between 1970 and 2009. These researchers found that the water level residuals in the study area were caused mainly by nonlinear changes in tidal constituents. Carless et al. (2016) investigated the response of tidally driven processes on the Patagonian Shelf to SLR using the Oregon State University Tidal Inversion Software (OTIS). These researchers found that the simulations with uniform SLR provided a different and slightly larger result than did a run where SLR was based on observed trends. Kuang et al. (2016) also used the Mike 21 model to investigate the potential influences of future SLR on tides in the China Sea. Their study indicated that large amplitude changes occurred at port locations as a result of SLR. A possible mechanism of tidal change might be related to decreasing bottom friction from increasing water depths due to SLR, migrating amphidromic points, and changing resonance effects. Idier et al. (2017) applied a validated shallow-water hydrodynamic model to investigate the effects of SLR on the western European Continental Shelf tide for a wide range of SLR values from -0.25 to 10 m. The results indicated that changes in the M_2 amplitudes reached SLR values of ± 15%. The changes in tidal water levels were different from the changes in M_2 amplitudes. The SLR-induced tidal changes resulted from the competition between the reduction in bed friction damping, changes in resonance properties and increased reflection at the coast. Wilmes et al. (2017) investigated the principal semidiurnal (M_2) tidal amplitude and energy dissipation responses to the nonuniform sea level changes induced by complete ice sheet collapses. The simulated results indicated global and spatially heterogeneous changes in tidal amplitudes. Schindelegger et al. (2018) modeled global effects of SLR on tides and managed to capture the observed signal accurately.

Taiwan is an island located between the continental shelf of mainland China and the open sea of the Pacific Ocean (Fig. 1a). Taiwan is subject to severe sea states induced by typhoons generated during summer in either the South China Sea or the Northwest Pacific Ocean near the Philippine islands, resulting in extensive loss of property and life. The marine geographical formation at the east coast of Taiwan facing the Pacific Ocean consists of rocks and gravel with steep bottom slopes up to the order of 1 m in 10 m, while the formation on the west coast along the Taiwan Strait consists of finer sands with much milder slopes of the order of approximately 1 m in 200–500 m. During the typhoon events, the west coast of Taiwan is often suffering from flooding and inundation. The sea level rise and typhoon invasion would aggravate the flooding and inundation in the future (Lewis et al., 2013, 2014).

Tide has been the dominant force in driving the hydrodynamics in the Taiwan Strait. The M_2 tide is the dominant astronomical tide, with the maximum amplitude (~2 m) appearing in the middle portion of the Taiwan Strait. Hwung et al. (1986) attributed these results to the encounter of two incident tidal waves, each from an opposite end of the strait. The maximum and minimum mean tidal ranges are 4.1 m and 0.69 m, respectively, located at Taichung Harbor and Kaohsiung Harbor.

The storm surge simulation and tide-surge prediction along the coast of Taiwan have been investigated using the fine horizontal resolution (Huang et al., 2007; Zhang et al., 2007; Li et al., 2009). However, tides and storm surges modulated by the SLR in the coastal regime of Taiwan have not been investigated using numerical models. The main objective of this study is to investigate the SLR influence on tides and storm surges around the coast of Taiwan using the ADCIRC (Advanced Circulation Model for Oceanic, Coastal and Estuarine Waters) model. The model was calibrated and validated using measured water levels, surge heights, air pressures, and wind speeds for different typhoon events. The validated model was then applied to investigate the effects of SRL on tides and surge heights and to quantify the nonlinear effects of the tide and surge interaction under the SLR scenario.

2. Materials and methods

2.1. Storm surge model

The ADCIRC storm surge model (Luettich et al., 1992) was used in this study to simulate the water levels in response to SLR along the Taiwan coast. Compared to other numerical models used to study the tides and storm surges along the Taiwan coast, the ADCIRC model takes advantage of source code, open access, and easy operation. The model has been widely used in the world to carry out the simulations of tides, storm surges, flooding, and wind driven circulation (e.g., Salisbury and Hagen, 2007; Chen et al., 2008; Bacopoulos et al., 2009; Hagen et al., 2012; Bhaskaran et al., 2014; Gayathri et al., 2016; Feng et al., 2018; Valle et al., 2018). In this region, the barotropic dynamics are dominant, and baroclinic effects are assumed to be relatively small during typhoon events (Huang et al., 2007; Zhang et al., 2007; Li et al., 2009). Therefore, the two-dimensional, depth-integrated ADCIRC model (ADCIRC-2DDI) is used in the present study. The two-dimensional version of the ADCIRC solves the depth-integrated, nonlinear momentum and continuity equations in the time domain. ADCIRC utilizes the continuous Galerkin finite-element method, which provides flexibility for resolving complex geometries and bathymetries in coastal areas.

The governing equations are discretized in space by finite elements and in time by a finite difference scheme (Luettich et al., 1992). The finite-element solution for the shallow water equations induces spurious terms and numerical instabilities. Hence, reformulating the governing equations into a form that provides a stable finite-element solution is necessary. ADCIRC-2DDI adopts the generalized wave continuity equation (GWCE) combined with momentum conservation equations to eliminate this issue (Westerink et al., 1994). The result is a noise-free solution that is applied to solve for the deviation from the free surface elevation related to the geoid and velocities in the x and y directions.

Frictional closure within the governing equations of ADCIRC is achieved within the use of a hybrid formulation of the standard quadratic bottom friction parameterization which allows for the bottom friction to change with respect to bathymetric depth. The default values for hybrid bottom friction parameters recommended by Murray (2003): $C_{f\ \min} = 0.0025$; $H_{break} = 1$ m; $\alpha = 10$; and $\beta = 1/3$. Horizontal eddy viscosity is 5.0 m^2/s.

The tidal energy loss includes the loss induced by bed friction and tidal conversion (Wilmes et al., 2017). The tidal conversion was not considered in the ADCIRC model. Therefore, the tidal energy loss would be underestimated, causing the calculated velocity field to be slightly

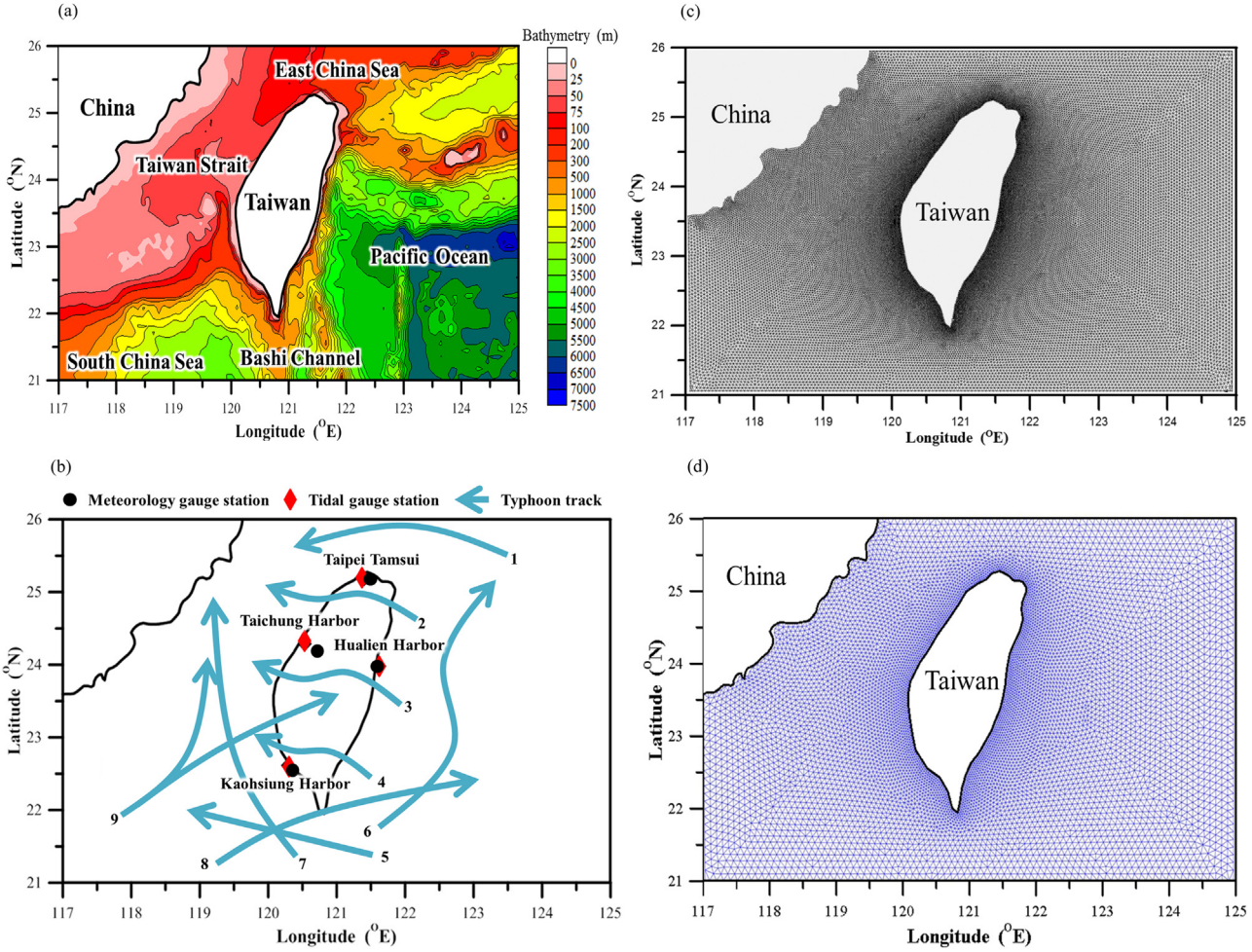

Fig. 1. (a) Bathymetric map, (b) locations of tidal and meteorology gauge stations along the coast of Taiwan and categorized paths from the Central Weather Bureau of Taiwan, (c) fine unstructured grids, and (d) coarse unstructured grids in the modeling domain for the simulation.

Table 1
Periods, landfall dates, paths, and intensities of the seven typhoon events used for the model calibration and validation.

Typhoon event	Model calibration				Model validation		
	Typhoon Mindulle	Typhoon Nanmadol	Typhoon Longwang	Typhoon Kaemi	Typhoon Wipha	Typhoon Jangmi	Typhoon Fanapi
Period (month/ day /year)	6/28/2004~ 7/4/2004	12/3/2004~ 12/4/2004	9/30/2005~ 10/3/2005	7/23/2006~ 7/26/2006	9/17/2007~ 9/19/2007	9/26/2008~ 9/29/2008	9/17/2010~ 9/20/2010
Landfall date	7/1/2004	12/4/2004	10/1/2005	7/24/2006	9/18/2007	9/28/2008	9/19/2010
Path	6	9	3	3	1	2	4
Intensity	Middle	Middle	Strong	Middle	Middle	Strong	Middle

higher.

The model forcing include the surface elevation at the open boundary, a zero land boundary flux, spatially and temporally variable free surface winds, and the atmospheric pressure. The model is capable of handling wetting and drying in low-lying areas. Numerous applications of this model by the U.S. Army Corps of Engineers and other institutions have been reported in the literature (e.g., Dietrich et al., 2011; Murty et al., 2014; Bhaskaran et al., 2014).

2.2. Wind and pressure field model

Storm surges are driven mainly by wind stresses and pressure fields. Several approaches are used to simulate the wind stress and pressure field of a typhoon. For example, Shen et al. (2006) and Liu et al. (2013) used SLOSH (Sea, Lake and Overland Surge from Hurricane model, Jelesnianski et al., 1992) to calculate the wind and pressure fields of a hurricane. Rao et al. (2013) solved the equations of wind and pressure to yield wind and pressure fields that were used to drive the hydrodynamic model.

To simplify the numerical calculation scheme, the pressure fields and wind fields are derived from independent formulas. The atmospheric pressure field for a cyclone was calculated using the equation expressed below (Holland, 1980):

$$p_a = p_c + \Delta p \cdot \exp[-(\frac{r}{r_m})^{-B}], \quad \Delta p = p_e - p_c, \quad r > 0 \tag{1}$$

where p_c is the ambient pressure or environmental pressure, Δp is the pressure drop or pressure deficit, r is the radius, which is the distance from the typhoon center, r_m is the radius of the maximum wind speed, and B is the shape parameter, which can be estimated according to the

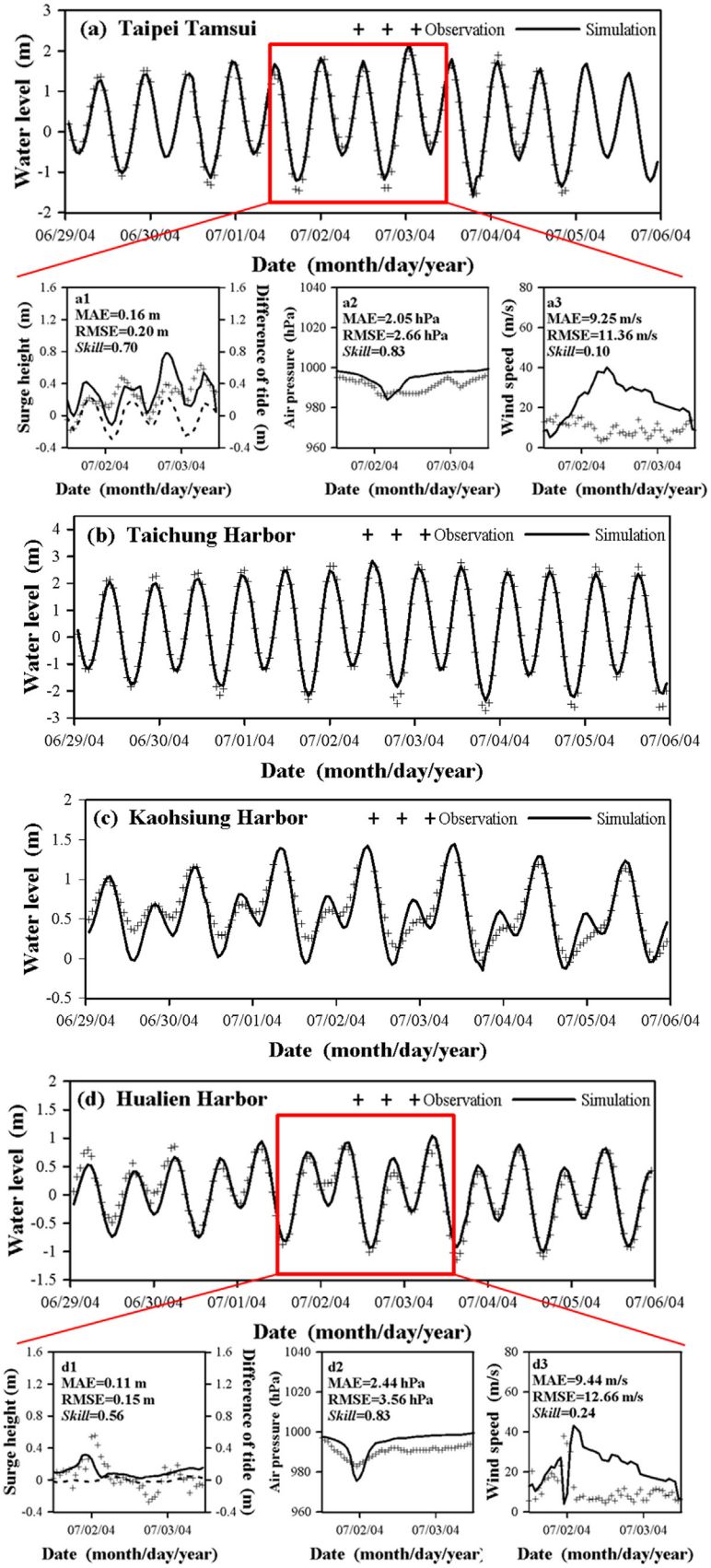

Fig. 2. Comparison between the modeled and observed water levels for model calibration with Typhoon Mindulle (2004) (typhoon path 6). Fig. (a1-a3) and (d1-d3) include a comparison between the modeled and observed surge height, air pressure, and wind speed. Note that the dashed line in Fig. a1 and Fig. d1 represents the surge signal when the air pressures and wind fields during typhoons are excluded in model simulations.

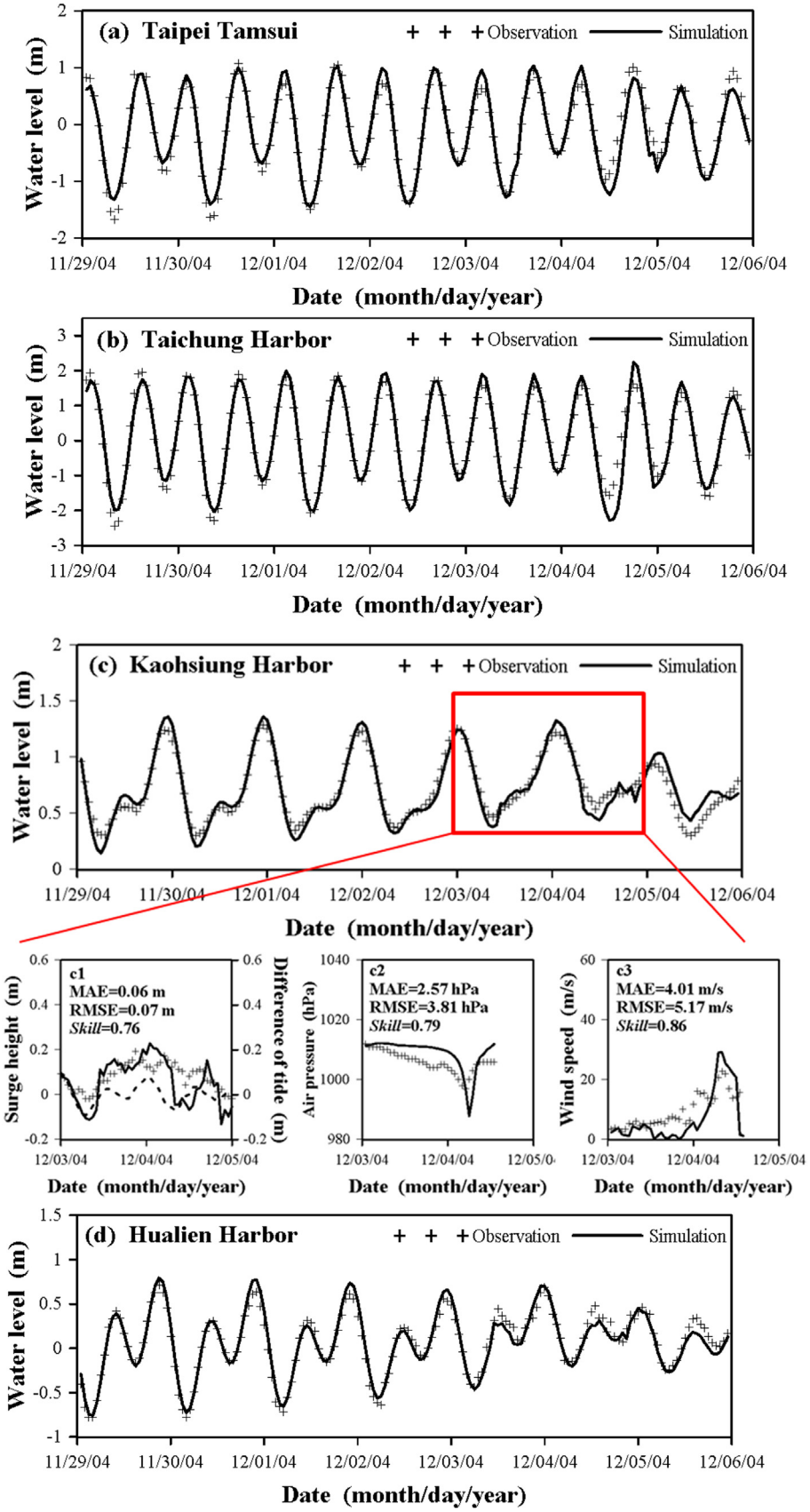

Fig. 3. A comparison between the modeled and observed water levels for model calibration with Typhoon Nanmadol (2004) (typhoon path 9). Fig. (c1-c3) include the comparison between the modeled and observed surge height, air pressure, and wind speed. Note that the dashed line in Fig. c1 represents the surge signal when the air pressures and wind fields during typhoons are excluded in model simulations.

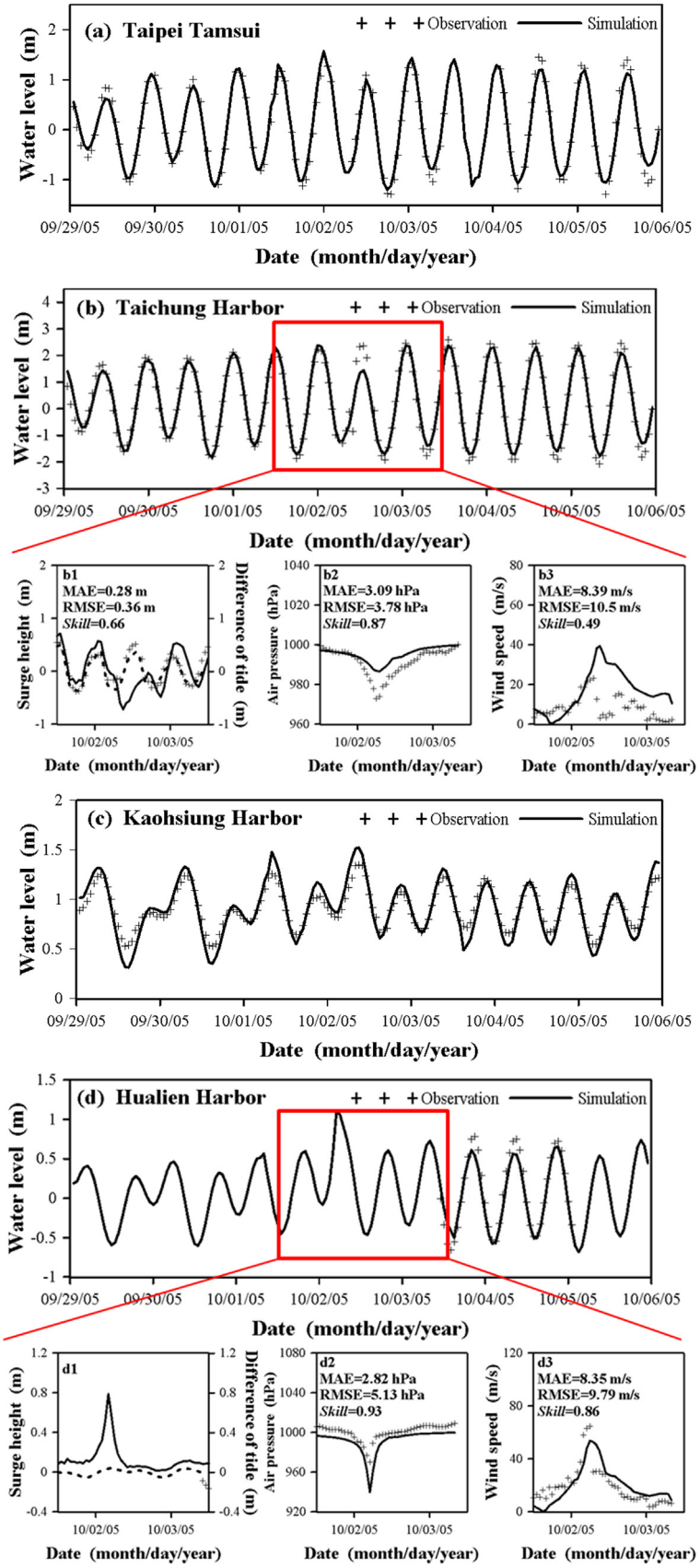

Fig. 4. A comparison between the modeled and observed water levels for model calibration with Typhoon Longwang (2005) (typhoon path 3). Fig. (b1-b3) and (d1-d3) include the comparison between the modeled and observed surge height, air pressure, and wind speed. Note that the dashed line in Fig. b1 and Fig. d1 represents the surge signal when the air pressures and wind fields during typhoons are excluded in model simulations.

Table 2
Mean absolute error (MAE), root mean square error (RMSE), and skill values of the differences between the computed and observed water levels for model calibration and model validation (using fine unstructured grids).

Model calibration												
Gauge station	Mindulle (2004)			Nanmadol (2004)			Longwang (2005)			Kaemi (2006)		
	MAE (m)	RMSE (m)	Skill	MAE (m)	RMSE (m)	Skill	MAE (m)	RMSE (m)	Skill	MAE (m)	RMSE (m)	Skill
Taipei Tamsui	0.13	0.17	0.99	0.13	0.16	0.99	0.12	0.14	0.99	0.12	0.15	0.99
Taichung Harbor	0.16	0.20	0.99	0.15	0.19	0.99	0.16	0.24	0.99	0.16	0.22	0.99
Kaohsiung Harbor	0.14	0.17	0.93	0.07	0.08	0.98	0.08	0.09	0.96	0.13	0.17	0.94
Hualien Harbor	0.13	0.16	0.98	0.07	0.08	0.99	0.08	0.09	0.99	0.08	0.10	0.99
Model validation												
Gauge station	Wipha (2007)			Jangmi (2008)			Fanapi (2010)					
	MAE (m)	RMSE (m)	Skill	MAE (m)	RMSE (m)	Skill	MAE (m)	RMSE (m)	Skill			
Taipei Tamsui	0.12	0.16	0.99	0.13	0.17	0.99	0.12	0.15	0.99			
Taichung Harbor	0.18	0.23	0.99	0.18	0.24	0.99	0.20	0.27	0.99			
Kaohsiung Harbor	0.08	0.10	0.95	0.10	0.13	0.95	0.12	0.15	0.92			
Hualien Harbor	0.10	0.12	0.97	0.10	0.14	0.97	0.09	0.12	0.96			

following empirical relationship (Jakobsen and Madsen, 2004):

$$B = 0.1397(\Delta p)^{0.288}, \quad r > 0 \tag{2}$$

where r is equal to zero, p_a is set to p_c and the maximum wind speed is set to zero.

Although typhoons possess different shapes, they can all be expressed as circular storms over the ocean. The circular wind and pressure field model of Jelesnianski (1965) is widely used in many tropical cyclone surge models. This model is used to calculate the wind field as follows:

$$\overrightarrow{W} = \frac{r}{r_m + r}(U_w i + V_w j) + W_m \frac{1}{r}\left(\frac{r}{r_m}\right)^{3/2}(ai + bj), \quad 0 < r \le r_m \tag{3}$$

$$\overrightarrow{W} = \frac{r_m}{r_m + r}(U_w i + V_w j) + W_m \frac{1}{r}\left(\frac{r_m}{r}\right)^{1/2}(ai + bj), \quad r > r_m \tag{4}$$

$$a = -r_\lambda \sin\theta - r_\varphi \cos\theta, \quad b = r_\lambda \cos\theta - r_\varphi \sin\theta$$

where (i, j) are the longitude and latitude unit vectors, respectively, U_w, V_w are the translation velocity components of the cyclone center, W_m is the maximum wind, r_λ and r_φ are the components of vector **r**, and θ is the inflow angle in the range 0–30°.

The longitude and latitude of the typhoon center, pressure at the typhoon center and maximum wind of the different typhoon paths (i.e., typhoon locations) were obtained from the Central Weather Bureau, Taiwan and input into a wind and pressure field model to yield the wind and pressure fields for different typhoon events, which were used to drive the ADCIRC model simulations.

2.3. Initial and boundary conditions

For the initial condition, the tidal current simulation starts with constant values (cold start) for the water level (mean sea level) and flow velocity (zero). The ramp-up period after the cold start is 10 days. The coastlines are considered to be no-flow closing boundaries because no-slip land boundary conditions are used in the model simulation.

To simulate tidal propagation in the ADCIRC model, driving tidal force at the open boundaries is necessary. In the present study, a global ocean tidal model that was developed by Oregon State University, which is the TOPEX/Poseidon Global Inverse Solution (TPXO) (http://volkov.oce.orst.edu/tides/), is used to specify the open boundaries of the ADCIRC for simulating tidal propagation. The TPXO incorporates data from the TOPEX/Poseidon satellite. The tides are provided as complex amplitudes of the earth-relative sea-surface elevation for eight primary (M_2, S_2, N_2, K_2, K_1, O_1, P_1, and Q_1) and two long-period (M_f and M_m) harmonic constituents. The details regarding the methods used to compute the model can be found in Egbert et al. (1994) and Egbert and Erofeeva (2002).

2.4. Model implementation

The computational domain included the region within longitudes 117°E to 125°E and latitudes 21°N to 28°N, which encompasses the Asian marginal seas and western Pacific Ocean. The digital terrain model (DTM) bathymetric data were obtained from the global topography database of the University of California at San Diego (http://ssdb.iodp.org/index.php) and from the Ocean Data Bank of the Ministry of Science and Technology, Taiwan (http://www.odb.ntu.edu.tw/bathy/?page_id=17). Fig. 1a and b show the bathymetry map and locations of tidal and meteorology gauge stations on the eastern and western coasts of Taiwan, respectively. The unsmoothed bathymetric data (shown in Fig. 1a) are used to generate numerical girds for model simulations. According to the Central Weather Bureau of Taiwan, the paths of the low-pressure center for typhoons with wind fields having physically affected the island are divided into nine categorized paths, which are shown in Fig. 1b.

To provide the grid for the model simulation, coarse grids were generated in coastal seas, and fine grids were used in shallower areas close to the coastline. The software SMS (surface water model system, https://www.aquaveo.com/) was used to generate the meshes. The coarse grid reaches 10 km and the finest grid is approximately 2 km. The modeling domain consisted of 74,124 unstructured triangular elements and 37,639 nodes (Fig. 1c). To compare the simulation results using fine and coarse unstructured grids, the coarse grids in the modeling domain were generated to consist of 15,677 unstructured triangular elements and 8093 nodes (Fig. 1d). The time step in the ADCRIC model is limited by CFL (Courant-Friedrichs-Lewy) criteria due to the semi-implicit formulation. Based on the model grids generated for the coastal ocean around Taiwan, a time step of $\Delta t = 20$ s was adopted in the simulations to guarantee the stability of the model.

2.5. Model performance

The model was quantitatively assessed using three criteria, which were adopted to compare the predicted results with the observational data. These criteria are the mean absolute error (MAE), root mean square error (RMSE), and skill, which are defined by the following equations:

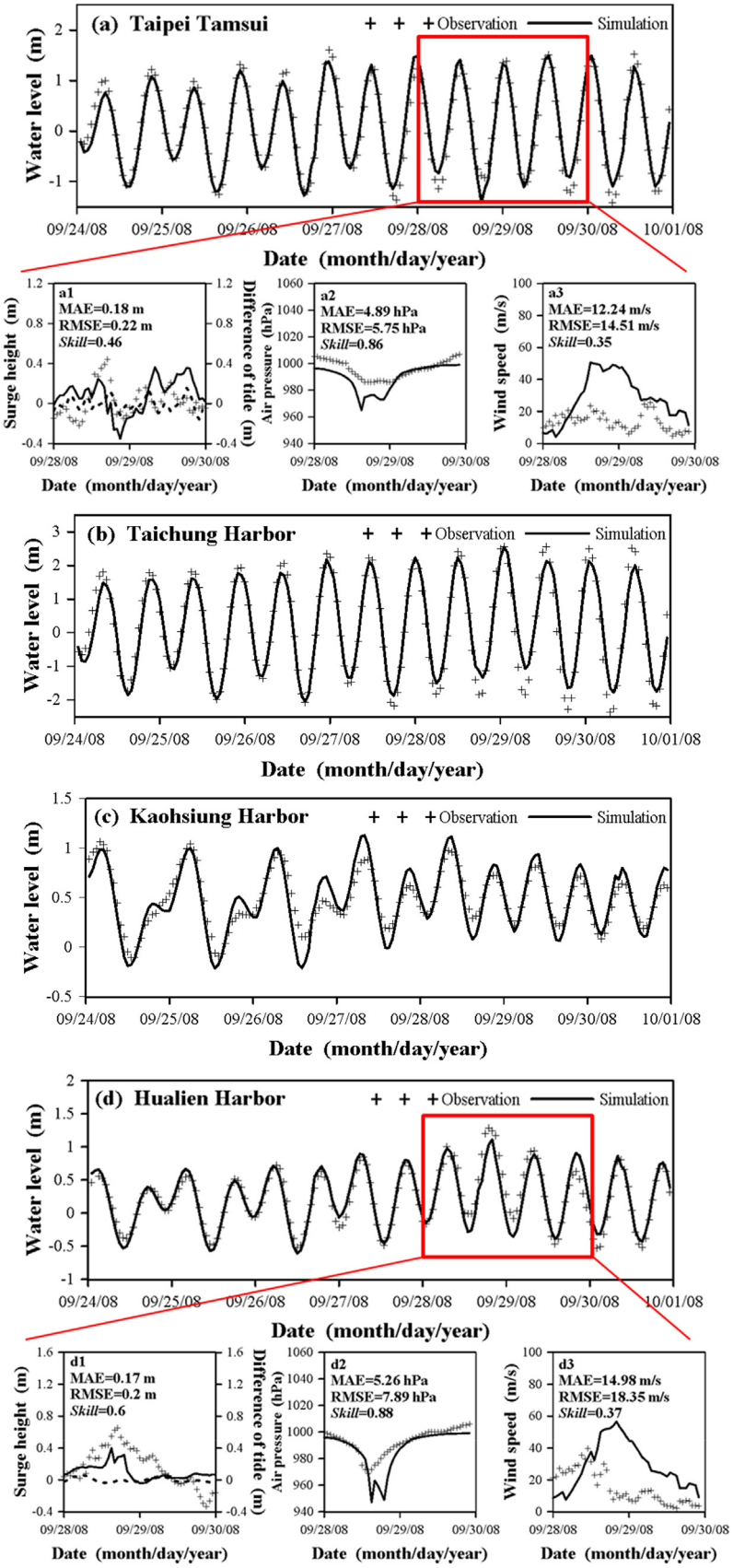

Fig. 5. A comparison between the modeled and observed water levels for model validation with Typhoon Jangmi (2008) (typhoon path 2). Fig. (a1-a3) and (d1-d3) include the comparison between the modeled and observed surge height, air pressure, and wind speed. Note that the dashed line in Fig. a1 and Fig. d1 represents the surge signal when the air pressures and wind fields during typhoons are excluded in model simulations.

Table 3
Mean absolute error (MAE), root mean square error (RMSE), and skill values of the differences between the computed and observed water levels for model calibration and model validation (using coarse unstructured grids).

Model calibration												
Gauge station	Mindulle			Nanmadol			Longwang			Kaemi		
	(2004)			(2004)			(2005)			(2006)		
	MAE (m)	RMSE (m)	Skill	MAE (m)	RMSE (m)	Skill	MAE (m)	RMSE (m)	Skill	MAE (m)	RMSE (m)	Skill
Taipei Tamsui	0.15	0.18	0.99	0.14	0.17	0.98	0.15	0.18	0.98	0.14	0.17	0.98
Taichung Harbor	0.17	0.22	0.98	0.17	0.25	0.98	0.20	0.27	0.98	0.20	0.26	0.98
Kaohsiung Harbor	0.16	0.20	0.91	0.08	0.09	0.97	0.09	0.10	0.95	0.14	0.18	0.93
Hualien Harbor	0.14	0.18	0.97	0.09	0.11	0.97	0.09	0.11	0.97	0.09	0.11	0.98
Model validation												
Gauge station	Wipha (2007)			Jangmi (2008)			Fanapi (2010)					
	MAE (m)	RMSE (m)	Skill	MAE (m)	RMSE (m)	Skill	MAE (m)	RMSE (m)	Skill			
Taipei Tamsui	0.14	0.17	0.98	0.15	0.19	0.98	0.13	0.16	0.98			
Taichung Harbor	0.19	0.24	0.98	0.21	0.26	0.98	0.24	0.29	0.98			
Kaohsiung Harbor	0.10	0.12	0.92	0.11	0.15	0.94	0.13	0.16	0.91			
Hualien Harbor	0.11	0.15	0.95	0.13	0.19	0.95	0.11	0.14	0.95			

$$MAE = \frac{1}{N}\sum_{i=1}^{N} |(Y_m)_i - (Y_o)_i| \tag{5}$$

$$RMSE = \sqrt{\frac{1}{N}\sum_{i=1}^{N} [(Y_m)_i - (Y_o)_i]^2}, \tag{6}$$

$$\text{Skill} = 1 - \frac{\sum_{i=1}^{N} |(Y_m)_i - (Y_o)_i|^2}{\sum_{i=1}^{N} [|(Y_m)_i - \overline{Y_o}| + |(Y_o)_i - \overline{Y_o}|]^2} \tag{7}$$

where N is the total number of data points, Y_m is the predicted water level, Y_o is the observed water level, and $\overline{Y_o}$ is the mean value of the observed water level. A skill value of 1.0 indicates a perfect model performance, a skill value between 0.65 and 1 indicates an excellent performance, a skill value in the range of 0.5–0.65 denotes very good performance, a skill value in the range of 0.2–0.5 suggests good performance, and a skill value of less than 0.2 indicates poor performance (Chen et al., 2016).

3. Model calibration and validation

Several sets of observational data were used to determine the model accuracy and to validate the predictive capabilities of the model. The observed data of water level for historical typhoon events were collected from the Central Weather Bureau, Taiwan. The unsmoothed observational data were used to calibrate and validate the model. There are several parameters in the ADCRIC model that require adjustment, including the horizontal eddy viscosity, bottom friction coefficient, break depth, and two dimensionless parameters (α and β). α is the parameter that establishes how rapidly the bottom friction factor approaches its upper and lower limits, and β is the parameter that describes how quickly the bottom friction factor increases as water depth decreases. These two dimensionless parameters affecting the bottom friction factor are to be determined. By trial and error, these parameters can be determined through model calibration and verification procedures. In this phase, the fine unstructured grids in the modeling domain (Fig. 1c) were used to model simulations.

Four typhoon events, which include Typhoon Mindulle (2004), Typhoon Nanmadol (2004), Typhoon Longwang (2005), and Typhoon Kaemi (2006), were used for model calibration. Three typhoon events, which include Typhoon Wipha (2007), Typhoon Jangmi (2008), and Typhoon Fanapi (2010), were used for model validation. Table 1 shows the periods, landfall dates, paths, and intensities of these seven typhoon events.

The tidal simulation and storm tide modeling results for the model calibration in terms of water levels during typhoon events, including Typhoon Mindulle (typhoon path 6), Typhoon Nanmadol (typhoon path 9), and Typhoon Longwang (typhoon path 3) (see Fig. 1b), are shown in Figs. 2–4. The comparisons of computed surge height, air pressure, and wind speed, as well as the observational results at some stations, are shown in the figures. These figures reveal that the model reasonably simulated both the spatial and temporal patterns of the tides and storm surges. Because the simulated wind fields were used to force the model, the slight differences between the model simulations and observations at some stations were found. The computed wind speeds did not reproduce the observations (see Figs. 2a3, d3, and 4b3). Overall, the simulated water levels, surge heights, and air pressures agree well with the observations. Table 2 shows the model performance between the computed and observed water levels for the model calibration. The maximum MAE and RMSE values are 0.16 m and 0.24 m, respectively, at Taichung Harbor for Typhoon Longwang. Meanwhile, the model skill value reached 0.99.

Fig. 5 presents the model validation results for the tides and storm surges in terms of the water level during Typhoon Jangmi (2008) (typhoon path 2). The comparisons of computed surge height, air pressure, and wind speed, as well as the observational results at some stations during typhoon periods, are also shown in the figure. The model results are unable to effectively describe the observed water levels and surge heights at some stations during the storm surge, possibly for the same reason that the wind and pressure field model was unable to reflect the observed wind speeds (see Fig. 5a3 and d3). However, the computed air pressures reproduced the observational results well. Note that the air pressures and wind fields were calculated from the wind and pressure field model (see Section 2.2). Table 2 also presents the model performance between the computed and observed water levels for model validation. The maximum MAE and RMSE values are 0.20 and 0.27 m, respectively, at Taichung Harbor for Typhoon Fanapi, but the model skill value also reaches 0.99. Moreover, the simulated results with the experimental test also reveal that the surge signals are not caught when the air pressures and wind fields during typhoons are excluded in model simulations. The simulated results can be found in Fig. 2a1 and d1, Fig. 3c1, Fig. 4b1 and d1, and Fig. 5a1 and d1 (dashed line).

Based on the abovementioned model calibration and validation procedures, the horizontal eddy viscosity parameter was set to 5.0 m^2/s. A constant minimum bottom friction coefficient of $C_{f\,\min} = 0.003$ was

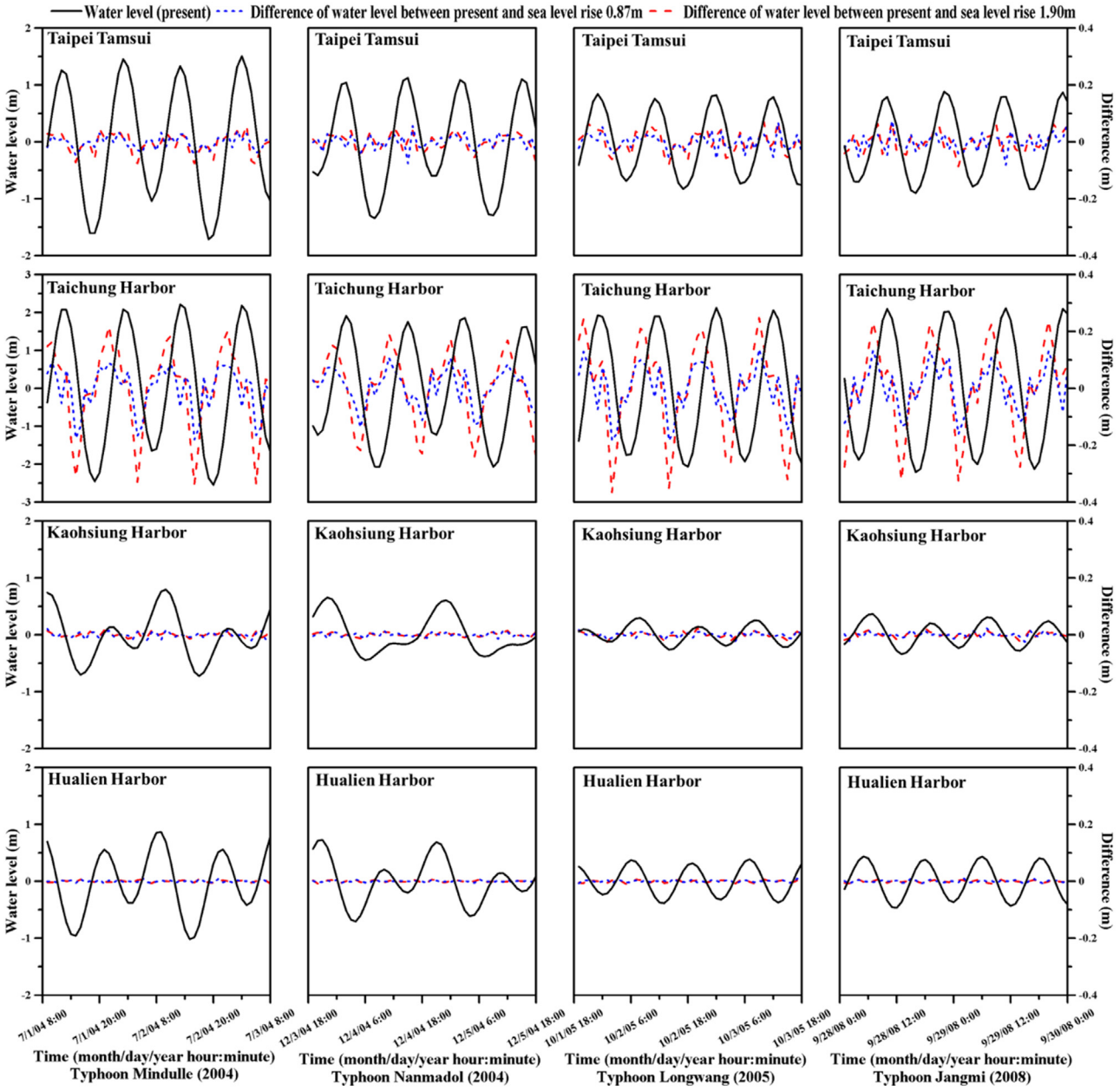

Fig. 6. Time-series of the water level and differences in the tides induced by sea level rises at Taipei Tamsui, Taichung Harbor, Kaohsiung Harbor, and Hualien Harbor. The changes caused by sea level rise are drawn in blue (+0.87 m) and red (+1.9 m). The black lines represent the time-series of the water level for present-day conditions (baseline). The columns from left to right represent Typhoon Mindulle (2004), Typhoon Nanmadol (2004), Typhoon Longwang (2005), and Typhoon Jangmi (2008).

also used in addition to a break depth of $H_{break} = 10$ m and two dimensionless parameters of $\alpha = 10$ and $\beta = 1/3$. The parameters used in this study are within the reasonable ranges found in Luettich et al. (1992).

To compare the model calibration and validation results using fine and coarse unstructured grids, the coarse grids were then applied to model simulations using same parameters in the model. Table 3 shows the model performance between the computed and observed water levels for model calibration and validation using coarse unstructured grids. Compared to simulation results in Table 2 (using fine unstructured grids), the model performance using coarse unstructured grids is poorer than the model performance using fine unstructured grids. Therefore, the fine unstructured grids are used for further model applications.

4. Model applications and discussion

To the best of our knowledge, there was no report to analyze the responses of sea level rise on the tides and surges around the Taiwan coast. Therefore, the validated model was then used to investigate the influence of sea level rise on the tides and surges around the coast of Taiwan. The SLR projections for the 21st century vary widely and range from several centimeters to more than a meter, which results in great future flood risk uncertainty for other regions (Lewis et al., 2011). According to different reports from the literature (Rahmstorf et al., 2007; Katsman et al., 2008), we selected two relative sea level rise scenarios, which included sea level rises of 0.87 m and 1.9 m and are projected to 2100 in the model simulations.

Two different approaches project the SLR for model simulations: increasing mean sea level by changing the bathymetry (Howard et al.,

Table 4
Maximum difference in the water levels and surge heights between present-day conditions and sea level rises of 0.87 m and 1.9 m.

Water level								
Gauge station	Maximum difference induced by sea level rise of 0.87 m (cm)				Maximum difference induced by sea level rise of 1.9 m (cm)			
	Mindulle (2004)	Nanmadol (2004)	Longwang (2005)	Jangmi (2008)	Mindulle (2004)	Nanmadol (2004)	Longwang (2005)	Jangmi (2008)
Taipei Tamsui	3.9	5.5	6.9	7.4	5.7	5.2	7.0	7.0
Taichung Harbor	9.2	10.8	13.7	13.3	21.8	19.2	24.8	23.7
Kaohsiung Harbor	2.1	1.4	1.7	2.3	1.6	1.5	2.4	2.3
Hualien Harbor	1.3	0.8	1.0	1.2	0.8	0.6	0.8	0.7
Surge height								
Gauge station	Maximum difference induced by sea level rise of 0.87 m (cm)				Maximum difference induced by sea level rise of 1.9 m (cm)			
	Mindulle (2004)	Nanmadol (2004)	Longwang (2005)	Jangmi (2008)	Mindulle (2004)	Nanmadol (2004)	Longwang (2005)	Jangmi (2008)
Taipei Tamsui	6.2	8.0	9.1	4.5	7.0	7.4	7.8	5.8
Taichung Harbor	8.3	9.6	14.9	5.9	7.1	8.2	13.3	10.4
Kaohsiung Harbor	2.2	1.6	2.3	1.2	1.5	2.1	9.9	1.2
Hualien Harbor	0. 9	1.3	1.3	2.6	0.8	1.0	1.2	1.0

2010; Zhao et al., 2014) and changing the open boundary conditions (Huang et al., 2015; Qiu and Zhu, 2015). The former assumes that the SLR is a uniform increase, and the latter assumes that the SLR induced from the deep sea and SLR across the domain is nonuniform. Because Taiwan is a small island, the spatial distribution of SLR is not considered. Therefore, in the present study, the impact of the SLR on the tides and storms is evaluated by adding 0.87 m and 1.9 m water depth to the present-day topography to represent future SLR scenarios.

Four typhoon events, which include Typhoon Mindulle (2004), Typhoon Nanmadol (2004), Typhoon Longwang (2005), and Typhoon Jangmi (2008), were used in the case study because the tracks of these typhoons are situated close to the four tidal gauge stations of Taipei Tamsui, Taichung Harbor, Kaohsiung Harbor, and Hualien Harbor. The combination of historical typhoons and SLR is the popular methodology used to form scenarios for further assessment (Ding et al., 2013; Zhao et al., 2014; Kung et al., 2017; Yin et al., 2017). Even though the same typhoon events will never occur again in the future, Taiwan is hit by a typhoon every year. Typhoon intensity and frequency will very likely increase.

4.1. Effects of sea level rise on the tides

To evaluate the effects of sea level rise on the tides, the typhoon model was excluded from the simulations during the typhoon events. Furthermore, the typhoon model was included in the model simulations during the typhoon events to assess the effects of seal level rise on the surges.

Fig. 6 presents the water level under present-day conditions and the differences in the water level between present-day and sea level rise conditions. The results show that the maximum differences in the water levels between present-day and sea level rise conditions of 0.87 m and 1.9 m at Taipei Tamsui, Taichung Harbor, Kaohsiung Harbor, and Hualien Harbor are all greater than 0.6 cm. A notable difference in the present-day water level and the water level for sea level rise conditions of 0.87 m and 1.9 m is observed at Taichung Harbor. There are small effects of sea level rise on the tides at Kaohsiung Harbor and Hualien Harbor because the maximum differences in the water levels are in the range of 0.6–2.4 cm under SLR of 0.87 m and 1.9 m (Table 4). The maximum differences in water levels under SLR of 0.87 m and 1.9 m range between 3.9 cm and 7.4 cm at Taipei Tamsui (Table 4). For changes in tides, the change caused by SLR 1.9 m (red line) is more obvious than the change caused by SLR 0.87 m (blue line) at Taichung Harbor. Zhao et al. (2014) also found an increasing trend as SLR increased around the Changjiang Estuary. The time-averaged difference for the difference of water level between present-day and SLR which is greater than zero ranges from 4.5 to 11.1 cm under sea level rise 0.87 m and 1.9 m at Taichung Harbor (see second panel of Fig. 6). However, the time-averaged difference at four gauge stations is almost zero. Table 4 shows the maximum differences in water levels between the present-day and sea level rise conditions of 0.87 m and 1.9 m at the tidal gauge stations. The maximum increase in the water level ranges from 9.2 cm to 13.7 cm under a sea level rise of 0.87 m and from 19.2 cm to 24.8 cm under a sea level rise of 1.9 m at Taichung Harbor. However, the influence of SLR on Taipei Tamsui is comparable to the influence of SLR on Taichung Harbor (See Fig. 6 and Table 4).

An obvious discrepancy in the water level as a result of sea level rise is predicted at Taichung Harbor. The reason for this discrepancy may be that Taichung Harbor is located in the middle of the Taiwan Strait, and therefore, the tide is greatly affected by the tidal current of the Pacific Ocean. At high tide, the sea water flows into the Taiwan Strait from both the north and south ends and meets the trough in the central part of the Taiwan Strait. At the low tide, the sea water flows in the opposite direction. Therefore, the tidal range at Taichung Harbor is notable, mainly due to the tidal current resonance in the Taiwan Strait. Juang and Chiang (2003) confirmed that due to the significant influence of the continental shelf topography in the Taiwan Strait, the oscillation type of the tidal wave on the continental shelf topography clearly appears as a partially repeated standing wave, and the antinodes of the standing wave appear in the waters near Taichung Harbor. Therefore, the SLR raises the water level at Taichung Harbor. The topography and bathymetry could cause the changes in the water level as a result of sea level rise.

4.2. Effects of sea level rise on amplitude and phase of M2 tide

The harmonic analysis was used to yield tidal amplitudes and phases based on the simulated water levels under present-day, SLR 0.87 m, and SLR 1.9 m. The M_2 tidal amplitudes for the present-day conditions and the changes of M_2 tidal amplitude as a result of SLR 0.87 m and SLR 1.9 m are shown in Fig. 7. The M_2 tidal amplitudes are 0.85 m, 1.47 m, 0.26 m, and 0.44 m at Taipei Tamsui, Taichung Harbor, Kaohsiung Harbor, and Haulien Harbor under the present-day conditions (Fig. 7a). The simulated results in M_2 tidal amplitude are similar to the literature reported by Lin et al. (2001). Fig. 7a also shows that the highest M_2 tidal amplitude is 1.95 m at Xinghua Bay in mainland China.

The differences of M_2 tide amplitude between SLR 0.87 m and

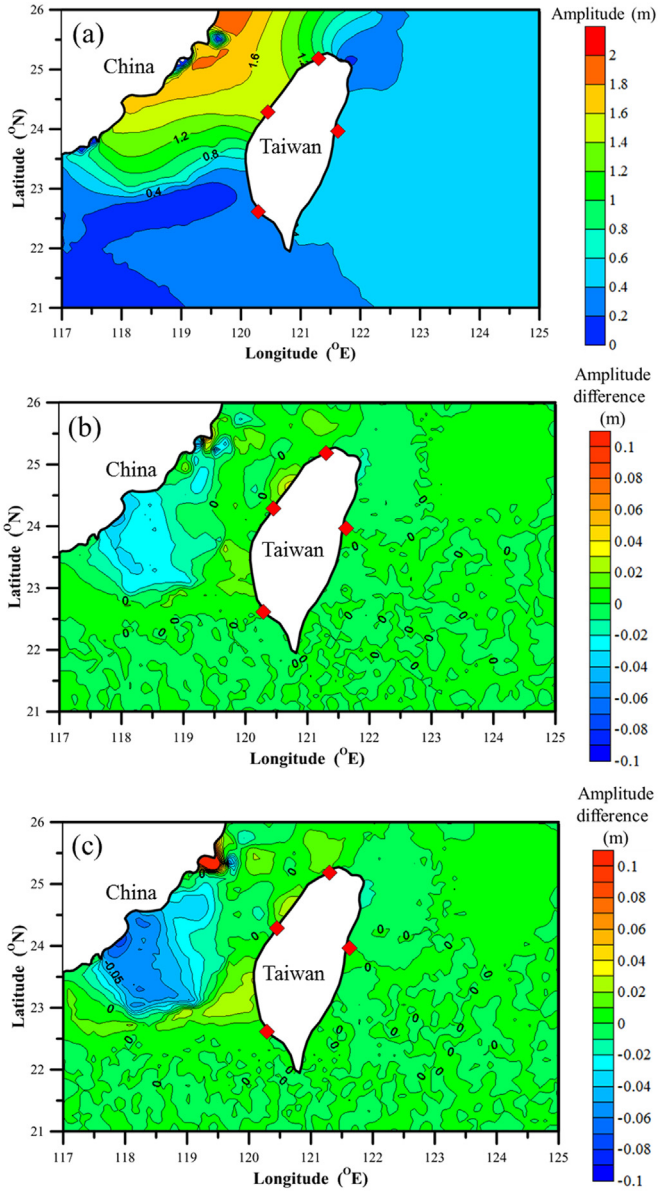

Fig. 7. (a) M_2 tidal amplitudes under present-day conditions and changes of the M_2 tidal amplitude caused by (b) SLR 0.87 m and (c) SLR 1.9 m.

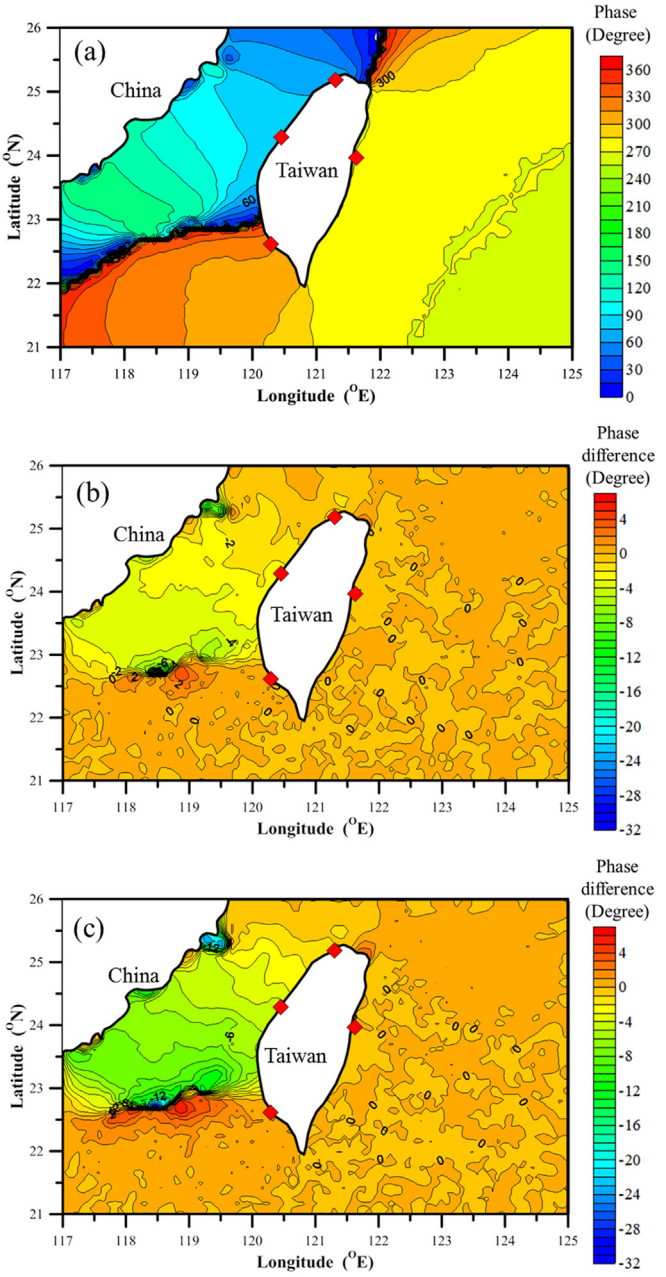

Fig. 8. (a) M_2 tidal phases under present-day conditions and changes of the M_2 tidal phase caused by (b) SLR 0.87 m and (c) SLR 1.9 m.

present-day conditions are 0.2 cm, 0.25 cm, 0.16 cm, and 0.03 cm at Taipei Tamsui, Taichung Harbor, Kaohsiung Harbor, and Haulien Harbor (Fig. 7b), while the differences between SLR 1.9 m and present-day conditions are 0.75 cm, 0.82 cm, 0.5 cm, and 0.1 cm (Fig. 7c). The changes in M_2 tidal amplitude are less than 1 cm due to sea level rise. However, the changes in M_2 tidal amplitude at Xinghua Bay in mainland China reach 8.1 cm and 21.8 cm due to SLR 0.87 m and 1.9 m, respectively.

The M_2 tidal phases for the present-day conditions and the changes of M_2 tidal phase as a result of SLR 0.87 m and SLR 1.9 m are shown in Fig. 8. The M_2 tidal phases are 66.8° (2.3 h), 83.6° (2.9 h), 320.6° (11.1 h), and 271.9° (9.4 h) at Taipei Tamsui, Taichung Harbor, Kaohsiung Harbor, and Haulien Harbor under the present-day conditions (Fig. 8a). The differences of M_2 tide phase between SLR 0.87 m and present-day condition are -1.22° (-2.5 min), -2.25° (-4.7 min), 0.16° (0.3 min), and -0.15° (-0.3 min) at Taipei Tamsui, Taichung Harbor, Kaohsiung Harbor, and Haulien Harbor (Fig. 8b), while the differences between SLR 1.9 m and present-day conditions are -1.32° (-2.7 min), -4.34° (-9 min), 0.72° (1.5 min), and -0.18° (0.4 min) (Fig. 8c). The abrupt change in bathymetry from deep to shallow around Kaohsiung coastal sea (see Fig. 1a) results in the late arrival of the M_2 tide at Kaohsiung Harbor due to sea level rise. The figure also indicates that the M_2 tide will arrive 4.7 min and 9 min earlier at Taichung Harbor as a result of SLR 0.87 m and 1.9 m, respectively.

Arns et al. (2015) documented that the effects of SLR-caused changes in the phase lags of individual constituents, thereby leading to a different tidal modulation as well as increasing the tidal water levels due to sea level rise. Howard et al. (2010) investigated the effects of high SLR values up to 5 m on the tides and surge heights at the Thames Estuary grid box (Southend) using the UK operational model. These researchers found that the primary effect was the tide timing, where the earlier arrival of approximately 1 h of high water had an effect on the water level of less than 10 cm. To investigate the effects of SLR on the tide timing, we recall that the motion of the tide belongs to the class of long gravity waves, and neglecting bottom friction, the tide is

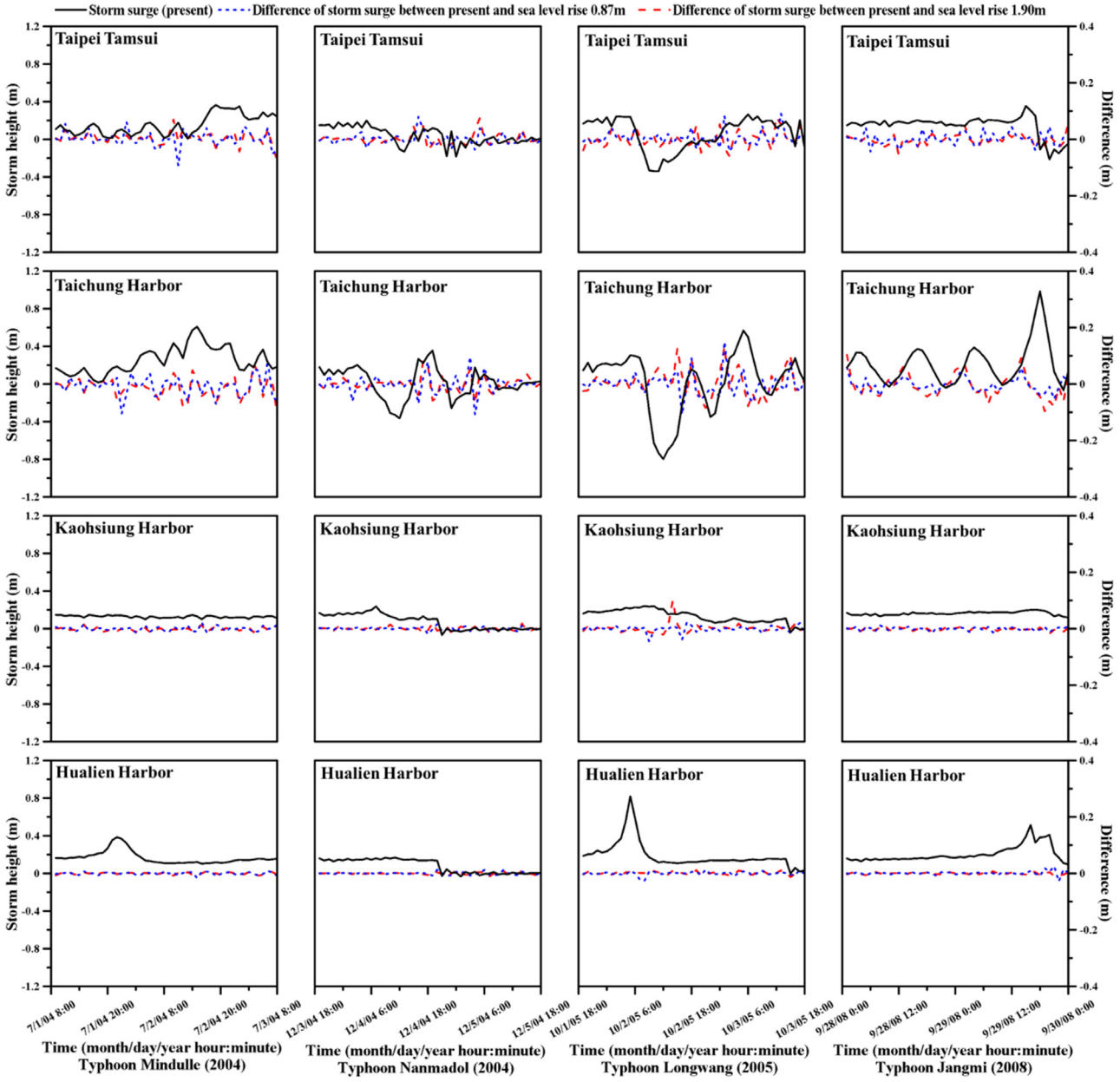

Fig. 9. A time-series of the surge height and differences in the surge heights induced by sea level rises at Taipei Tamsui, Taichung Harbor, Kaohsiung Harbor, and Hualien Harbor. The changes caused by sea level rise are drawn in blue (+0.87 m) and red (+1.9 m). The black lines represent the time-series of the surge height for present-day conditions (baseline). The columns from left to right represent Typhoon Mindulle (2004), Typhoon Nanmadol (2004), Typhoon Longwang (2005), and Typhoon Jangmi (2008).

approximated as a shallow water wave with wave speed $\sqrt{gh}$, where g is the gravitational acceleration, and h is the water depth. If the tidal current travels from the southern open boundary to Taichung Harbor (approximately 400 km) in 6 h, a shallow water wave speed of 18.53 m/s and a water depth of approximately 35 m result. Adding an SLR of 1.9 m (0.87 m) gives a new depth of 36.9 m (35.87 m) and yields a new shallow water wave speed of approximately 19 m/s (18.76 m/s), allowing the tide to arrive approximately 9 min (4.4 min) earlier at Taichung Harbor. We found that the numerical model results in changes of tidal phase at Taichung Harbor due to SLR 0.87 m and 1.9 m matched the results calculated by theoretical analysis.

4.3. Effects of sea level rise on surge heights

To predict the effects of sea level rise on surge heights, the wind and pressure field model was included in the typhoon event simulations. Fig. 9 illustrates the surge height time-series during the typhoon events and the differences in the surge heights induced by the sea level rise conditions of 0.87 m and 1.9 m. Fig. 9 shows that an obvious discrepancy in the surge heights induced by sea level rise can be found at Taichung Harbor, while there are no notable differences exhibited at Kaohsiung Harbor or Hualien Harbor. Table 4 also indicates the maximum differences in surge heights induced by sea level rise conditions of 0.87 m and 1.9 m at the tidal gauge stations. The maximum increase in the surge heights induced by a sea level rise of 0.87 m ranges from 5.9 cm to 14.9 cm, while the increase in the surge height induced by a sea level rise of 1.9 m ranges from 7.1 cm to 13.3 cm at Taichung Harbor. Gao et al. (2008) pointed out that the storm surge response to SLR is nonuniform spatially and changes as the typhoon processes differ.

Fig. 10(a)-(l) display the contours of the peak water levels under

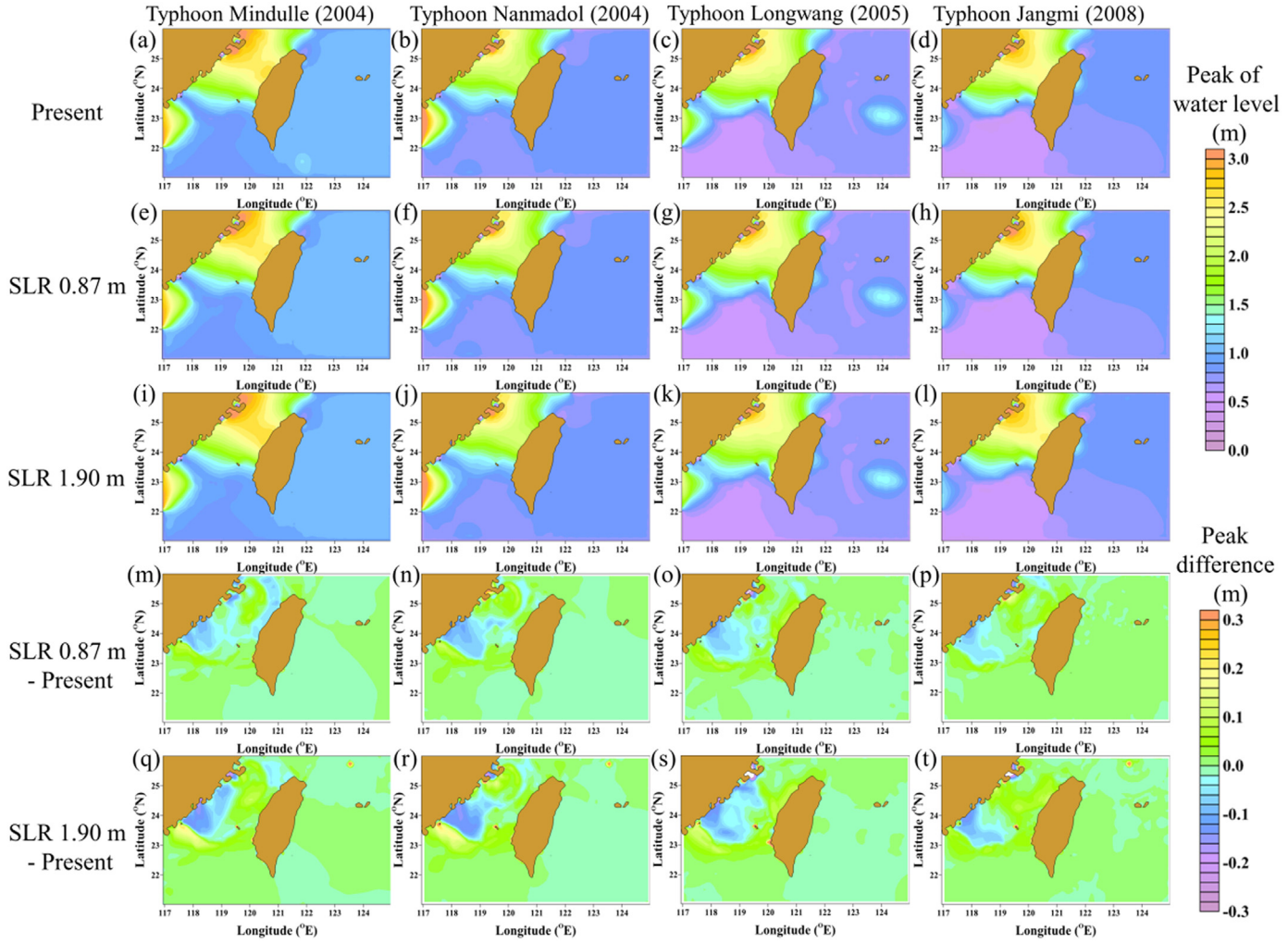

Fig. 10. Distribution of the peak water levels and their changes considering an SLR of 0.87 and an SLR of 1.9 m. Figures (a)-(l) show the peak water levels under present-day conditions under an SLR of 0.87 m and under an SLR of 1.9 m. Figures (m)-(t) represent increases in the peak water levels (i.e., a peak water level for an SLR of 0.87 m and an SLR of 1.9 m minus the peak water levels under present-day conditions). The columns from left to right represent Typhoon Mindulle (2004), Typhoon Nanmadol (2004), Typhoon Longwang (2005), and Typhoon Jangmi (2008).

present-day conditions, an SLR of 0.87 m, and an SLR of 1.9 m for different typhoon events. An increased rate of sea level rise cannot modify the basic distribution pattern of the peak water levels. The maximum peak water levels occur almost at the continental shelf between Taiwan and mainland China. The maximum peak water levels are located at Putian City and Xinghua Bay in mainland China where the peak water levels are above 2.8 m, possibly the reason that the areas are subjected to topographic and bathymetric effects. Because the bathymetry depends on the depth at the east and south coast of Taiwan compared to the west coast of Taiwan, the maximum peak water level ranges between 0.1 m and 1.5 m.

Fig. 10(m)-(t) present the contours of differences in the maximum water levels calculated by subtracting the maximum water level of each grid in the baseline case from the sea level rise condition cases of 0.87 m and 1.9 m for different typhoon events. The variations reveal nonlinear and nonuniform patterns around the coast of Taiwan. The difference in the peak water level decreases (see blue color) where the peak water level is located at the shallow continental shelf along the coast of mainland China, which may be subject to the topographic and bathymetric effects. The maximum difference in the peak water level increases from 0.102 m to 0.312 m under SLR of 0.87 m and from 0.157 m to 0.274 m under SLR of 1.9 m for four typhoon events. Therefore, the changes in the peak water levels are significant and cannot be neglected. These figures also indicate that the difference in the maximum water level along the eastern coast of Taiwan is less than the difference in the maximum water level along the western coast of Taiwan, possibly because tides and surges interact with the current between Taiwan and China (i.e., in the Taiwan Strait).

4.4. Effects of tide-surge interaction due to SLR

To quantify the nonlinear effects of the tide and surge interaction under SLR 1.90 m, the model was used with different experiments during Typhoon Jangmi (2008), which served as the case study. Three simulated scenarios were used in the experimental studies, including: (A) tidal boundaries only, (B) tidal boundaries + atmospheric forcing (including wind and air pressure forcing), and (C) no tidal boundaries + atmospheric forcing (including wind and air pressure forcing). Fig. 11 presents the modeling results for simulations A, B, and C. The water level for simulation B minus simulation A, which is designated as the surge height, is also presented in the figure. This figure shows that the timing of the peak surge height is quite different from the timing of the peak water level during simulation A and simulation B. This characteristic demonstrates the phase shift due to the tide-surge interaction. The surge heights are different for simulation C and simulation B minus simulation A due to the nonlinear advective and bottom friction effects, which have been demonstrated by Bernier and Thopmson (2007). Ding et al. (2013) and Bilskie et al. (2016) also confirmed that the

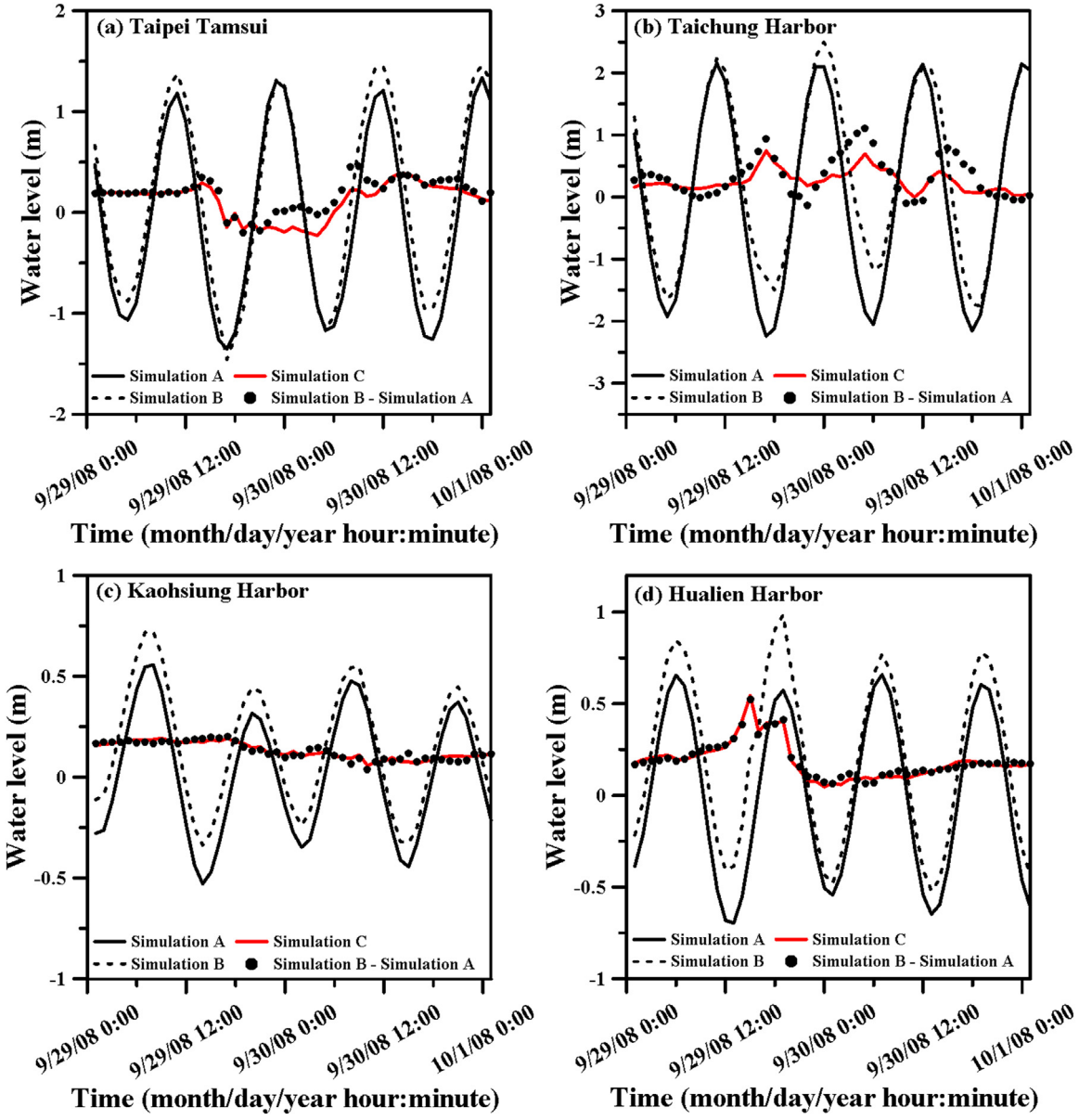

Fig. 11. Predicted water level using different simulations at (a) Taipei Tamsui, (b) Taichung Harbor, (c) Kaohsiung Harbor, and (d) Hualien Harbor.

interactions among SLR and storm surges are spatially and temporally nonlinear and that an increase in sea level would result in an earlier arrival of the peak surge.

4.5. General remarks

The methodology used in this study can be applied to other regions, although the continental shelf in Taiwan is smaller than other large shelves. A bigger difference would be found in different regions compared to the very little shelf in Taiwan, because long shallow regions would be modified tidal wave propagation (Lu Clara et al., 2015; Pickering et al., 2017). The model has been satisfactorily calibrated and validated with extensively measured data, thus we have great confidence that the validated model can be explored for the impact of SLR on tides and storm surges around the Taiwan coast. According to the analysis of tide-surge interaction as a result of SLR, an earlier arrival of the peak surge would cause a challenge on the early warning of storm surge. Shoreline changes result from changes of the morphology in the beach-dune system. These changes do not occur as a direct result of SLR, but as the response to tidal action, currents, waves, and sediment availability (Nicholls and Cazenave, 2010). However, in this study, shoreline changes in the continental shelf are not considered in the model. In the future study, the coupled storm surge and morphodynamic model will be used to investigate the effect of mobile sediment and shoreline changes with SLR on tides and storm surges.

5. Conclusions

A high-resolution, two-dimensional, hydrodynamic advanced circulation model (ADCIRC) with an unstructured grid was used to simulate tides and storm surges in the coastal seas of Taiwan. The TOPEX/Poseidon Global Inverse Solution (TPXO) global ocean tidal model developed by Oregon State University was applied to specify the ocean boundaries in ADCIRC to drive tidal propagation in the sea. A wind and pressure field model was used to simulate the wind stresses and pressure fields. Four typhoon events, which include Typhoon Mindulle (2004), Typhoon Nanmadol (2004), Typhoon Longwang (2005), and Typhoon Kaemi (2006), were used for model calibration. Meanwhile, three typhoon events, which include Typhoon Wipha (2007), Typhoon Jangmi (2008), and Typhoon Fanapi (2010), were

used for model validation. The results reveal a reasonable agreement between the model simulations and the observed data with respect to the tides and surge tides. To compare the simulation results using fine and coarse unstructured grids, the coarse grids were also used for model predictions. The results indicate that the model performance using coarse unstructured grids is poorer than the model performance using fine unstructured grids.

The validated model was then applied to investigate the effects of sea level rise on tides and surges using four typhoon events. According to the different reports from the literature, two sea level rise scenarios of 0.87 m and 1.9 m were used in the model simulations. The modeling results indicate that the water levels and surge heights at Taipei Tamsui, Taichung Harbor, Kaohsiung Harbor, and Hualien Harbor will increase due to sea level rise. Remarkable differences in the water levels and surge heights induced by sea level rise are observed at Taichung Harbor. The differences of M_2 tide amplitude between SLR 0.87 m and 1.9 m and present-day conditions are less than 1 cm at four gauge stations. SLR would cause the high tide to arrive approximately 9 min (4.7 min) earlier for SLR 1.9 m (0.87 m) at Taichung Harbor, showing that an increase in the water level would result in an increase in tidal wave propagation in coastal areas. By increasing the extent of sea level rise, the water level peak would become dangerous to coastal environments.

This study adds weight to existing knowledge regarding the necessary and rapid mitigation of climate change to prevent the impact of sea level rise such as saltwater intrusion, coastal flooding, shoreline erosion, and wetland migration (Karim and Mimura, 2008; Mcleod et al., 2010). Further research will incorporate a wave model into the tide-surge model to investigate the influences of different physical factors on the tide-surge and wave interactions.

Acknowledgements

The project under which this study was conducted was supported by the Ministry of Science and Technology (MOST) of Taiwan under grant no. 105-2625-M-239-001-MY2. The authors would like to express their appreciation to the Central Weather Bureau for providing the measurement data. The assistance of Prof. R. Luettich and Research Technician C. Fulcher, who provided the source code of the ADCIRC model, is also highly appreciated. Two anonymous reviewers are thanked for their constructive comments to substantially improve the paper.

References

Almas, A.J., Hygen, H.O., 2012. Impacts of sea level rise toward 2100 on buildings in Norway. Build. Res. Inf. 40, 245–259.
Arns, A., Wahl, T., Dangendorf, S., Jensen, J., 2015. The impact of sea level rise on storm surge water levels in the northern part of the German Bight. Coast. Eng. 96, 118–131.
Atkinson, J., Smith, J.M., Bender, C., 2013. Sea-level rise effects on storm surge and nearshore waves on the Texas Coast: Influence of landscape and storm characteristics. J. Waterw. Port Coast. Ocean Eng. 98–117.
Bacopoulos, P., Funakoshi, Y., Hagen, S.C., Cox, A.T., Cardone, V.J., 2009. The role of meteorological forcing on the St. Johns River (Northeastern Florida). J. Hydrol. 369, 55–70.
Bahar, D.B., Dyurgerov, M., Meier, M.F., 2009. Sea-level rise from glaciers and ice caps: a lower bound. Geophys. Res. Lett. 36, L03501.
Bernier, N.B., Thopmson, K.R., 2007. Tide-surge interaction off the east coast of Canada and northeastern United States. J. Geophys. 112, C06008.
Bhaskaran, P.K., Gayathri, R., Murty, P.L.N., Bonthu, S., Sen, D., 2014. A numerical study of coastal inundation and its validation for Thane cyclone in the Bay of Bengal. Coast. Eng. 83, 108–118.
Bilskie, M.V., Hagen, S.C., Medeiros, S.C., Passeri, D.L., 2014. Dynamics of sea level rise and coastal flooding on a changing landscape. Geophys. Res. Lett. 41, 927–934.
Bilskie, M.V., Hagen, S.C., Alizard, K., Medeiros, S.C., Passeri, D.L., Needham, H.F., Cox, A., 2016. Dynamic simulation and numerical analysis of hurricane storm surge under sea level rise with geomorphologic changes along the northern Gulf of Mexico. Earth's Future 4, 177–193.
Bittermann, K., Rahmstorf, S., Perrette, M., Vermeer, M., 2013. Predictability of twentieth century sea-level rise from past data. Environ. Res. Lett. 8, 014013.
Carless, S.J., Green, J.A.M., Pelling, H.E., Wilmes, S.B., 2016. Effects of future sea-level rise on tidal processes on the Patagonian Shelf. J. Mar. Syst. 163, 113–124.
Chen, Q., Wang, L., Tawes, R., 2008. Hydrodynamic response of northeastern Gulf of Mexico to hurricanes. Estuar. Coast. 31, 1098–1116.
Chen, W., Chen, K., Kung, C., Zhu, D.Z., He, L., Mao, X., Ling, H., Song, H., 2016. Influence of sea level rise on saline water intrusion in the Yangtz River Estuary, China. Appl. Ocean Res. 54, 12–25.
Cheon, S., Suh, K., 2016. Effect of sea level rise on nearshore significant waves and coastal structures. Ocean Eng. 114, 280–289.
Church, J.A., Clark, P.U., Cazenave, A., Gregory, J.M., Jevrejeva, S., Levermann, A., Merrifiled, M.A., Miline, G.A., Nerem, R.S., Nunn, P.D., Payne, A.J., Pfeffer, W.T., Stammer, D., Unnikrishnan, A.S., 2013. Sea level change. In: Stocker, T.F. et al. (eds), Climate Change 2013: the Physical Science Basis. Contribution on Working Group I to the Fifth Assessment Report of the Intergovernmental Panel on Climate Change. Cambridge University Press, Cambridge, United Kingdom and New York, NY, USA, p 1140.
Church, J.A., White, N., 2006. A 20th century acceleration in global sea-level rise. Geophys. Res. Lett. 33, L01602.
Church, J.A., White, N., 2011. Sea-level rise from the late 19th to the early 21 century. Surv. Geophys. 32, 585–602.
Craft, C., Clough, J., Ehman, J., Joye, S., Park, R., Pennings, S., Guo, H., Machmuller, M., 2009. Forecasting the effects of accelerated sea-level rise on tidal marsh ecosystem services source. Front. Ecol. Environ. 7, 73–78.
Dietrich, J.D., Zijlema, M., Westerink, J.J., Holthuijsen, L.H., Dawson, C., Luettich, R.A., Jensen, R.E., Smith, J.M., Stelling, G.S., Stone, G.W., 2011. Modeling hurricane waves and storm surge using integrally-coupled, scalable computations. Coast. Eng. 58, 45–65.
Ding, Y., Kuiry, S.N., Elgohry, M., Jia, Y., Altinakar, M.S., Yeh, K.C., 2013. Impact assessment of sea-level rise and hazardous storm on coasts and estuaries using integrated processes model. Ocean Eng. 71, 74–95.
Egbert, G.D., Bennett, A.F., Foreman, M.G., 1994. TOPEX/POSEIDON tides estimated using a global inverse model. J. Geophys. Res. 99, 24821–24852.
Egbert, G.D., Erofeeva, S.Y., 2002. Efficient inverse modeling of barotropic ocean tides. J. Atmos. Ocean. Tech. 19, 183–204.
Feng, X., Li, M., Yin, B., Yang, D., Yang, H., 2018. Study of storm surge trends in typhoon-prone coastal areas based on observations and surge-wave coupled simulation. Int. J. Appl. Earth Obs. Geoinf. 68, 272–278.
Gao, Z.G., Han, S.Z., Liu, K.X., Zheng, Y.X., Yu, H.M., 2008. Numerical simulation of the influence of mean sea level rise on typhoon storm surge in the east China Sea. Mar. Sci. Bull. 10, 36–49.
Gayathri, R., Murty, P.L.N., Bhaskaran, P.K., Kumar, T.S., 2016. A numerical study of hypothetical storm surge and coastal inundation for AILA cyclone in the Bay of Bengal. Environ. Fluid Mech. 16, 429–452.
Grinsted, A., Moore, J.C., Jevrejeva, S., 2010. Reconstructing sea level from paleo and projected temperatures 200 to 2100 AD. Clim. Dyn. 34, 461–472.
Gregory, J.M., Oerlemans, J., 1998. Simulated future sea-level rise due to glacier melt based on regionally and seasonally resolved temperature changes. Nature 391, 474–476.
Hagen, S.C., Bacopoulos, P., 2012. Coastal flooding in Florida's big bend region with application to sea level rise based on synthetic storms analysis. Terr. Atmos. Ocean Sci. 23, 481–500.
Hagen, S.C., Bacopoulos, P., Cox, A.T., Cardone, V.J., 2012. Hydrodynamics of the 2004 Florida Hurricanes. J. Coast. Res. 28, 1121–1129.
Holland, G.J., 1980. An analytic model of the wind and pressure profiles in hurricanes. Mon. Weather Rev. 108, 1212–1218.
Howard, T., Lowe, J., Horsburgh, K., 2010. Interpreting century-scale changes in southern North Sea storm surge climate derived from coupled model simulations. J. Clim. 23, 6234–6247.
Huang, W.P., Hsu, C.A., Kung, C.S., Yim, J.Z., 2007. Numerical studies on typhoon surges in the Northern Taiwan. Coast. Eng. 54, 883–894.
Huang, W., Hagen, S., Bacopoulos, P., Wang, D., 2015. Hydrodynamic modeling and analysis of sea-level rise impacts on salinity for oyster growth in Apalachicola Bay, Florida. Estuar. Coast. Shelf Sci. 156, 7–18.
Hwung, H.H., Tsai, C.L., Wu, C.C., 1986. Studies on the correlation of tidal elevation changes along the western coastline of Taiwan. In Proceedings of Coastal Engineering, pp. 293–305, Taipei, Taiwan.
Idier, D., Paris, F., Le Cozannet, G., Boulahya, F., Dumas, F., 2017. Sea-level rise impacts on the tides of the European Shelf. Cont. Shelf Res. 137, 56–71.
Jakobsen, F., Madsen, H., 2004. Comparison and further development of parametric tropical cyclone models for storm surge modelling. J. Wind Eng. Ind. Aerod. 92, 375–391.
Jay, D.A., 2009. Evolution of tidal amplitudes in the eastern Pacific Ocean. Geophys. Res. Lett. 36, L04603.
Jelesnianski, C.P., 1965. A numerical calculation of storm tides induced y a tropical storm impinging on a continental shelf. Mon. Weather Rev. 93, 343–358.
Jelesnianski, C.P., Chen, J., Shaffer, W.A., 1992. SLOSH: Sea, Lake, and Overland Surges from Hurricane. National Weather Service, Silver Springs, MD.
Juang, W.J., Chiang, C.C., 2003. Confirmation of the tidal oscillation patterns in the Taiwan Strait. Proceeding of the 25th Ocean Eng. Taiwan, pp. 31–38.
Karim, M.F., Mimura, N., 2008. Impact of climate change and sea-level rise on cyclonic storm surge floods in Bangladesh. Glob. Environ. Change 18, 490–500.
Katsman, C.A., Hazeleger, W., Drijfhout, S.S., van Oldenborgh, G.J., Bugers, G., 2008. Climate scenarios of sea level rise for the northeast Atlantic Ocean: a study including the effects of ocean dynamics and gravity changes induced by ice melt. Clim. Change 91, 351–374.
Kuang, C., Liang, H., Mao, X., Karney, B., Gu, J., Huang, H., Chen, W., Song, H., 2016. Influence of potential future sea-level rise on tides in the China Sea. J. Coast. Res. 33, 105–117.

Lewis, M., Bates, P., Horsburgh, K., Neal, J., Schumann, G., 2013. A storm surge inundation model of the northern Bay of Bengal using publicly available data. Q. J. R. Meteorol. Soc. 139, 358–369.
Lewis, M., Horsburgh, K., Bates, P., 2014. Bay of Bengal cyclone extreme level estimate uncertainty. Nat. Hazard. 72, 983–996.
Lewis, M., Horsburgh, K., Bates, P., Smith, R., 2011. Quantifying the uncertainty in future coastal flood risk estimates for the U.K. J. Coast. Res. 27, 870–881.
Li, H.W., Tsai, C.H., Lo, Y.T., 2009. Numeri cal simulation of typhoon surges along the coast of Taiwan. Nat. Hazard. 50, 413–431.
Liu, H., Zhang, K., Li, Y., Xie, L., 2013. Numerical study of the sensitivity of mangroves in reducing storm surge and flooding to hurricane characteristics in southern Florida. Cont. Shelf Res. 64, 51–65.
Lin, M.C., Juang, W.J., Tsay, T.K., 2001. Anomalous amplifications of semidiurnal tides along the western coast of Taiwan. Ocean Eng. 28, 1171–1198.
Lopes, C.L., Dias, J.M., 2014. Influence of mean sea level rise on tidal dynamics of the Ria de Aveiro lagoon, Portugal. J. Coast. Res. SI 70, 574–579.
Luettich, R.A., Westerink, J.J., Scheffner, N.W., 1992. ADCIRC: An advanced three-dimensional circulation model for shelves, coasts, and estuaries, Report I: theory and methodology of ADCIRC-2DDI and ADCIRC-3DL, US Army Corps of Engineers, Technical Report DRP-92-96.
Luz Clara, M., Simionato, C.G., D'Onofrio, E., Moreira, D., 2015. Future sea level rise and changes on tides in the Patagonian Continental Shelf. J. Coast. Res. 31, 519–535.
Mather, A.A., Stretch, D.D., 2012. A perspective on sea level rise and coastal storm surge from southern and eastern Africa: a case study near Durban, South Africa. Water 4, 237–259.
Mcleod, E., Poulter, B., Hinkel, J., Reyes, E., Salm, R., 2010. Sea-level rise impact models and environmental conservation: a review of models and their applications. Ocean Coast. Manag. 53, 507–517.
Muller, M., Arbic, B.K., Mitrovica, J.X., 2011. Secular trends in ocean tides: observation and model results. J. Geophys. Res. 116, C05013.
Murray, R.R., 2003. A Sensitivity Analysis for a Tidally Influenced Riverine System (MS thesis). University of Central Florida, Orlando, Florida.
Murty, P.L.N., Sandhya, K.G., Bhaskaran, P.K., Jose, F., Gayathri, R., Balakrishnan Nair, T.H., Kumar, T.S., Shenoi, S.S.C., 2014. A coupled hydrodynamic modeling system for PHAILIN cyclone in the Bay of Bengal. Coast Eng. 93, 71–81.
Nicholls, R.J., Cazenave, A., 2010. Sea-level rise and its impact on coastal zones. Science 328, 1517–1520.
Pelling, H.E., Mattias Green, J.A., Ward, S.L., 2013. Modelling tides and sea-level rise: to flood or not to flood. Ocean Model. 63, 21–29.
Pfeffer, W.T., Harper, J.T., O'Neel, S., 2008. Kinematic constraints on glacier contributions to 21-century sea-level rise. Science 321, 1340–1343.
Pickering, M.D., Horsburgh, K.J., Blundell, J.R., Hirschi, J.J.M., Nicholls, R.J., Verlaan, M., Wells, N.C., 2017. The impact of future sea-level rise on the global tides. Cont. Shelf Res. 142, 50–68.
Pickering, M.D., Wells, N.C., Horsburgh, K.J., Green, J.A.M., 2012. The impact of future sea-level rise on the European Shelf tides. Cont. Shelf Res. 35, 1–15.
Qiu, C., Zhu, J., 2015. Assessing the influence of sea level rise on salt transport processes and estuarine circulation in the Changjiang River estuary. J. Coast. Res. 31, 661–670.
Rahmstorf, S., 2007. A semi-empirical approach to projecting future sea-level rise. Science 315, 368–370.
Rao, A.D., Murty, P.L.N., Jian, I., Kankara, R.S., Dube, S.K., Murty, T.S., 2013. Simulation of water levels and extent of coastal inundation due to a cyclone storm along the east coast of India. Nat. Hazards 66, 1431–1441.
Raper, S.C.B., Braithwaite, R.J., 2006. Low sea level rise projections from mountain glaciers and icecaps under global warming. Nature 439, 311–313.
Ray, R.D., 2006. Secular changes of the M2 tide in the Gulf of Maine. Cont. Shelf Res. 26, 422–427.
Ray, R.D., 2009. Secular changes in the solar semidiurnal tide of the western North Atlantic Ocean. Geophys. Res. Lett. 36, L19601.
Salisbury, M.B., Hagen, S.C., 2007. The effect of tidal inlets on open storm surge hydrographs. Coast. Eng. 54, 377–391.
Schindelegger, M., Green, J.A.M., Wilmes, S.B., Haigh, I.D., 2018. Can we model the effect of observed sea level rise on tides? J. Geophys. Res. Oceans.
Shen, J., Wang, H., Sisson, M., Gong, W., 2006. Storm tide simulation in the Chesapeake Bay using and unstructured grid model. Estuar. Coast. Shelf Sci. 68, 1–16.
Sheng, Y.P., Paramygin, V.A., Terng, C.T., Chu, C.H., 2016. Simulating storm surge and inundation along the Taiwan coast during typhoons Fanapi in 2010 and Soulik in 2013. Terr. Atmos. Ocean Sci. 27, 965–979.
Tang, H.S., Chien, I-Jy, S., Temimi, M., Blain, C.A., Qu, K., Zhao, L.H., Kraatz, S., 2013. Vulnerability of population and transportation infrastructure at the east bank of Delaware Bay due to coastal flooding in sea-level rise conditions. Nat. Hazards 69, 141–163.
Testut, L., Duvat, D., Ballu, V., Fernandes, R.M.S., Pouget, F., Salmon, C., Dyment, J., 2016. Shoreline changes in a rising sea level context: the example of Grande Glorieuse Scattered Island, western Indian Ocean. Acta Oecol. 72, 110–119.
Tseng, Y.H., Breaker, L.C., Chang, E.T.Y., 2010. Sea level variations in the regional seas around Taiwan. J. Oceanogr. 66, 27–39.
Valle, A.N.R., Curchitser, E.N., Bruyere, C.L., Fossell, K.R., 2018. Simulating storm surge impacts with a coupled atmosphere-inundation model with varying meteorological forcing. J. Mar. Sci. Eng. 6, 35.
Ward, S.L., Green, J.A.M., Pelling, H.E., 2012. Tides, sea-level rises and tidal power extraction on the European shelf. Ocean Dyn. 62, 1153–1167.
Westerink, J.J., Luettich, R.A., Blain, C.A., Scheffner, N.W., 1994. ADCIRC: An Advanced Three-dimensional Circulation Model for Shelves, Coasts and Estuaries. Report 2: Users' Manual for ADCIRC-2DDI. U.S. Army Corps of Engineers (Technical Report, DRP-94).
Wilmes, S.B., Green, J.A.M., Gomez, N., Rippeth, T.P., Lau, H., 2017. Global tidal impacts of large-scale ice sheet collapses. J. Geophys. Res. Oceans 122, 8354–8370.
Woodworth, P.L., 2010. A survey of recent changes in the main components of the ocean tide. Cont. Shelf Res. 30, 1680–1691.
Yin, K., Xu, S., Huang, W., Xie, Y., 2017. Effects of sea level rise and typhoon intensity on storm surge and waves in Pearl River Estuary. Ocean Eng. 136, 80–93.
Zhang, W.Z., Hong, H.S., Shang, S.P., Chen, D.W., Chai, F., 2007. A two-way nested coupled tide-surge model for the Taiwan Strait. Cont. Shelf Res. 27, 1548–1567.
Zhao, C., Ge, J., Ding, P., 2014. Impact of sea level rise on storm surges around the Changjiang Estuary. J. Coast. Res. SI 68, 27–34.
Zuo, Z., Oerlemans, J., 1997. Contribution of glacier melt to sea-level rise since AD 1865: a regionally differentiated calculation. Clim. Dyn. 13, 835–845.